

# Nanoscale

Accepted Manuscript



This is an *Accepted Manuscript*, which has been through the Royal Society of Chemistry peer review process and has been accepted for publication.

*Accepted Manuscripts* are published online shortly after acceptance, before technical editing, formatting and proof reading. Using this free service, authors can make their results available to the community, in citable form, before we publish the edited article. We will replace this *Accepted Manuscript* with the edited and formatted *Advance Article* as soon as it is available.

You can find more information about *Accepted Manuscripts* in the [Information for Authors](#).

Please note that technical editing may introduce minor changes to the text and/or graphics, which may alter content. The journal's standard [Terms & Conditions](#) and the [Ethical guidelines](#) still apply. In no event shall the Royal Society of Chemistry be held responsible for any errors or omissions in this *Accepted Manuscript* or any consequences arising from the use of any information it contains.

Cite this: DOI: 10.1039/c0xx00000x

www.rsc.org/xxxxxx

**PAPER**

# Alteration of architecture of MoO<sub>3</sub> nanostructures on arbitrary substrates: growth kinetics, spectroscopic and gas sensing properties

Navas Illyaskutty,<sup>\*a,b</sup> Sreeja Sreedhar,<sup>c</sup> G. Sanal Kumar,<sup>b</sup> Heinz Kohler,<sup>a</sup> Matthias Schwotzer,<sup>d</sup> Carsten Natzeck<sup>d</sup> and V.P. Mahadevan Pillai<sup>b</sup>

5 Received (in XXX, XXX) Xth XXXXXXXXXX 20XX, Accepted Xth XXXXXXXXXX 20XX

DOI: 10.1039/b000000x

MoO<sub>3</sub> nanostructures have been grown in thin film form on five different substrates by RF magnetron sputtering and subsequent annealing; non-aligned nanorods, aligned nanorods, bundled nanowires, vertical nanorods and nanoslabs are formed respectively on the glass, quartz, wafer, alumina and sapphire substrates. The nanostructures formed on these substrates are characterized by AFM, SEM, GIXRD, XPS, micro-Raman, diffuse reflectance and photoluminescence spectroscopy. A detailed growth model for morphology alteration *w. r. t.* substrates has been discussed by considering various aspects such as surface roughness, lattice parameters and thermal expansion coefficient of both substrates and MoO<sub>3</sub>. The present study brought out a strategy for the choice of substrates to materialize different types MoO<sub>3</sub> nanostructures for future thin film applications. The gas sensing tests point towards using these MoO<sub>3</sub> nanostructures as principal detection elements in gas sensors.

## 1. Introduction

Low dimensional metal oxide nanomaterials have stimulated great interest for basic scientific research due to their unique electrical, optical and mechanical properties as well as potential technological applications in nanodevices.<sup>1-4</sup> Among the metal oxides, molybdenum oxide (MoO<sub>3</sub>) comprises a vital position as it can form variety of morphologies such as nano-wires,<sup>5</sup> -rods,<sup>6</sup> -tubes,<sup>7</sup> -belts,<sup>8</sup> -fibers,<sup>9</sup> -ribbons,<sup>10</sup> -platelets,<sup>11</sup> -particles,<sup>12</sup> -flowers,<sup>13</sup> -whiskers,<sup>14</sup> -slabs,<sup>15</sup> -spheres,<sup>16</sup> -stars,<sup>17</sup> -flakes,<sup>18, 19</sup> -sheets<sup>20</sup> etc. due to its peculiar layered crystal structure that favours anisotropic growth. A substantial number of investigations have been focused in recent times on MoO<sub>3</sub> nanostructures due to their potential applications as electrochemical energy storage devices,<sup>1</sup> excellent field emitters,<sup>17</sup> gas sensors,<sup>21</sup> reversible lithium-ion batteries<sup>22</sup> and catalysts.<sup>23</sup> Because of the favourable electrical properties, molybdenum oxide crystal films can be used as solar cells and heated reflective films.<sup>24</sup> Moreover, it displays electro-, photo-

gaso-chromic coloration effects and dielectric properties<sup>25</sup>, which are useful for application in electro-chromic devices,<sup>26</sup> photo-chromic devices,<sup>27</sup> optical switching coatings,<sup>28</sup> panel displays<sup>29</sup> and smart windows.<sup>30</sup>

Most of the studies on the synthesis of molybdenum oxide nanostructures are focussed on electro-deposition<sup>1</sup>, thermal evaporation,<sup>5, 31</sup> wet-chemical methods such as hydrothermal or solvothermal synthesis,<sup>6-10, 32</sup> chemical vapour deposition,<sup>12, 15</sup> sonochemical,<sup>14</sup> direct heating of molybdenum foil in air,<sup>17, 33</sup> aqueous solution process,<sup>34</sup> laser assisted evaporation,<sup>35</sup> ultrasonic spray pyrolysis<sup>36</sup> etc. It is very significant to grow MoO<sub>3</sub> nanostructures in thin film form for several applications such as gas sensors, field emission devices, batteries and electro-chromic devices<sup>17-22</sup> etc. RF magnetron sputtering in excessive argon atmosphere and controlled subsequent calcination in atmospheric air is recognized as a method for the preparation of MoO<sub>3</sub> nanostructures on glass substrates by our previous studies.<sup>37-39</sup> The fabrication of MoO<sub>3</sub> nanostructures in thin film form on a substrate base is highly influenced by deposition method, nature of the substrates, deposition temperature, growth time, deposition pressure, vacuum quality, calcination temperature etc. A crucial challenge in this field is the choice of substrate since the nature of the substrate can alter the morphology and spectroscopic properties of the nanostructures due to thermal mismatch (owing to the difference in thermal expansion coefficients) and lattice mismatch between the substrates and MoO<sub>3</sub>,<sup>8, 30, 32</sup> therefore, a thorough understanding of the effects of substrates on the morphological, structural and optical properties of MoO<sub>3</sub> nanostructures is a prerequisite for the realization of nano-MoO<sub>3</sub> based applications.

<sup>a</sup>Institute for Sensorics and Information Systems (ISIS), Karlsruhe University of Applied Sciences, Moltekestr. 30, D-76133, Karlsruhe, Germany.

40 Fax: +497219251301, Tel: +497219251329, Email: navasillyas@gmail.com

<sup>b</sup>Department of Optoelectronics, University of Kerala, Kariavattom, Thiruvananthapuram-695581, Kerala, India.

<sup>c</sup>Department of Physics, University of Kerala, Kariavattom, 45 Thiruvananthapuram-695581, Kerala, India.

<sup>d</sup>Institute of Functional Interfaces (IFG), Karlsruhe Institute of Technology (KIT), Hermann-von-Helmholtz-Platz 1, D-76344 Eggenstein-Leopoldshafen, Karlsruhe, Germany.

In this paper, RF Magnetron sputtering and controlled subsequent annealing is employed to fabricate MoO<sub>3</sub> nanostructures with special attention paid to the effects of the nature of substrates on the structure, morphology and optical properties of MoO<sub>3</sub> nanostructures. Moreover, the feasibility of using the as-prepared nanostructures for gas sensing applications is also investigated.

## 2. Experimental

The deposition of MoO<sub>3</sub> nanostructures on five different substrates is performed by the RF magnetron sputtering system. Pressed MoO<sub>3</sub> powder (Merck, purity 99.99%) is used as target. The substrates used are amorphous soda lime glass, amorphous fused quartz, silicon wafer (100, n-type) and Al<sub>2</sub>O<sub>3</sub> in two forms: polycrystalline alumina (rough) and single-crystalline (0001) sapphire (polished). The base pressure in the chamber is maintained  $\sim 3 \times 10^{-6}$  mbar before sputtering and the deposition is carried out at high background argon pressure (0.07 - 0.1 mbar). The other sputtering parameters are optimized as substrate-target distance - 5 cm, R F power - 150 W operating at 13.56 MHz, deposition time - 30 minutes. The as-grown films are then annealed in air for 1 hour at 673 K by maintaining the raise and drop of temperature at a rate of 10 K/min and 5 K/min, respectively using a programmed furnace. The thickness of the films is determined by Tencor P-1 Long Scan Profiler and it varies in the range of 272-401 nm (Table 1).

The surface morphology of the nanostructured films are studied by atomic force microscopy (AFM-Digital Instruments Nanoscope E, with Si<sub>3</sub>N<sub>4</sub> 100 $\mu$ m cantilever, 0.58 N/m force constant) measurements in contact mode and scanning electron microscopy (SEM-Carl Zeiss DSM 942). The crystalline structure and crystallographic orientation of the MoO<sub>3</sub> nanostructures on different substrates are investigated by grazing-incidence X-ray diffraction (GIXRD) measurements using a Siemens D5000 diffractometer (operating at 40 kV and 25 mA) employing Cu K $\alpha$  radiation with a wavelength of 0.15406 nm in the range of  $2\theta = 10-45$ . Micro-Raman spectra of the films are recorded using a Horiba Jobin Yvon LABRAM-HR 800 Spectrometer of spectral resolution  $\sim 1$  cm<sup>-1</sup> equipped with an Ar<sup>+</sup> ion laser at an excitation wavelength, 488 nm. Diffuse reflectance UV-Vis spectra in the range of 200-500 nm is recorded by a JASCO V-550 UV-Vis spectrophotometer equipped with a diffuse reflectance attachment, using BaSO<sub>4</sub> as reference. Horiba Jobin Yvon Spectrofluorometer (Fluorolog III) equipped with Xenon lamp of 450 W and R928P photo-multiplier tube in photon counting mode as detector is used to record photoluminescence spectra. The cut-on and cut-off optical filters are used to remove the distortions caused by the second-order peaks or Rayleigh bands. All the spectra are recorded using an excitation wavelength of 250 nm. For the X-ray Photoelectron Spectroscopy (XPS) measurements, a hemispherical VG Scienta R4000 analyzer was used. An Al K $\alpha$  non-monochromatized radiation ( $h\nu = 1486.71$  eV) was employed as X-ray source. Survey spectra were recorded with a pass energy of 200 eV and high resolution spectra of the Mo3d, O1s, C1s core level regions was recorded with a pass energy of 100 eV. The peaks were fitted using a combination of Gaussian and Lorentzian curves and Marquardt-Levenberg optimization algorithm.

## 3. Results and Discussion

### 3.1. Morphological study and growth model

The Typical AFM images of MoO<sub>3</sub> nanostructures formed on five different substrates are shown in Fig 1. It is obvious from the figure that nature of substrate has a drastic influence on the morphology, dimension and orientation of the nanostructures. The films on the glass and quartz substrates exhibit uniformly distributed nanorods with smooth edges and well defined grain boundaries. On glass substrate, the nanorods are distributed without specific orientation, whereas, the nanorods on quartz substrate follow a specific orientation. The approximate length and diameter of the nanorods on glass and quartz substrates are determined to be  $\sim 600 \pm 25 \times 100 \pm 15$  nm and  $\sim 510 \pm 20 \times 80 \pm 10$  nm, respectively. The areal density of the MoO<sub>3</sub> nanorods on these substrates is  $\sim 10^5$  cm<sup>-2</sup>. However, longer nanowires of length  $\sim 1 \pm 0.05$   $\mu$ m and diameter  $\sim 40 \pm 10$  nm are formed on Si-wafer.

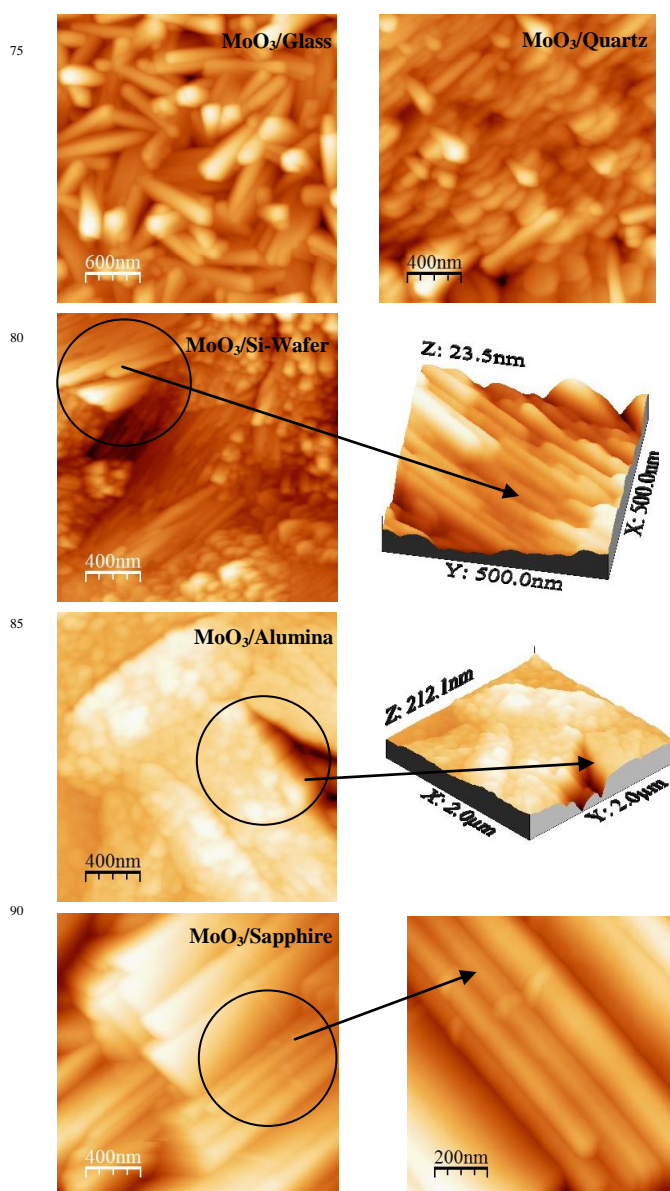


**Fig. 1** AFM images illustrating the formation of MoO<sub>3</sub> nanostructures on five different substrates.

On Si-wafer, the long nanowires are arranged in bundles and each bundle follows a specific orientation (Fig 1). On alumina substrate, nanorods of length  $\sim 220 \pm 15$  nm and diameter  $\sim 56 \pm 5$  nm are grown perpendicular to the substrate surface. The nanostructures formed on sapphire look like stacked nanoslabs which are uniformly distributed over the substrate. The nanoslabs are straight and have rectangular flat tips with four sharp corners at the upper ends and the facets are rectangular with round edges. The length, width and thickness of nanoslabs are  $\sim 2 \pm 0.1$   $\mu\text{m}$ ,  $290 \pm 15$  nm and  $80 \pm 10$  nm respectively. The nanoslabs show hubs at the middle which seems that two nanoslabs of length  $\sim 1 \pm 0.06$   $\mu\text{m}$  are connected together at that point. However, these nanostructures on all substrates except quartz are not well oriented; instead, they grow at certain tilted angles and it is due to the formation of tetrapod like junctions in nanorods. Defects in  $\text{MoO}_3$  nuclei can increase the chance of forming tetrapod like junctions, resulting in tilted nanorods.<sup>40</sup> The SEM studies (Fig 2) of the  $\text{MoO}_3$  films on different substrates ascertain the presence of nanostructures having similar morphology, dimension, crystal orientation and growth direction, as observed from the AFM micrographs.

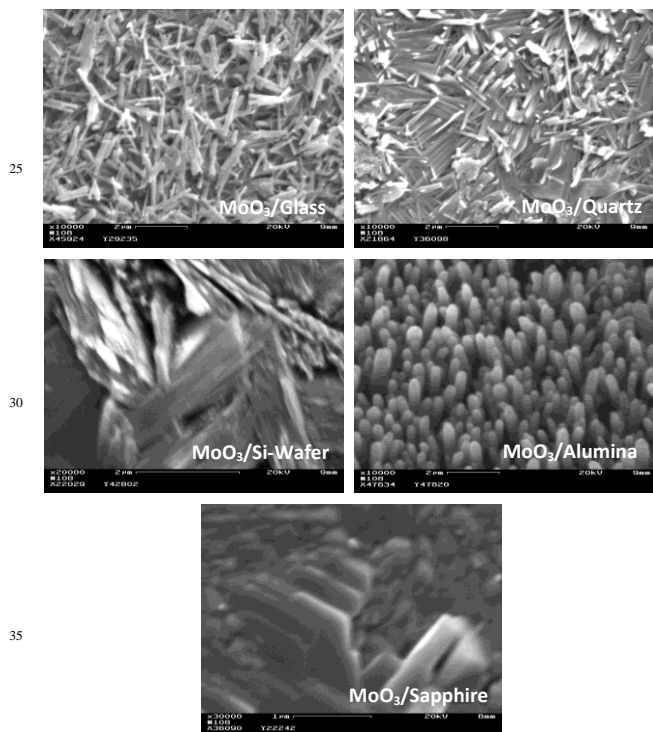


**Fig. 2** SEM images of the various  $\text{MoO}_3$  nanostructures formed on five different substrates.

The  $\text{MoO}_3$  nanostructures are believed to be formed by two processes (1) sputtering–re-deposition at high argon ambience during RF magnetron sputtering and (2) enhanced rearrangement during controlled subsequent calcination at 673 K. The elaborated discussion on the mechanism of formation of  $\text{MoO}_3$  nanorods can be found elsewhere.<sup>37–39</sup> However, the effect of substrates has driven a significant role in the structure, morphology and orientation of  $\text{MoO}_3$  nanostructures. In order to study the crystalline structure and crystallographic growth orientation of the  $\text{MoO}_3$  nanostructures on different substrates, grazing-incidence X-ray diffraction (GIXRD) measurements are performed.

The GIXRD patterns of the  $\text{MoO}_3$  nanostructures grown on various substrates are displayed in Fig. 3. All diffraction peaks are consistent with orthorhombic  $\alpha$ - $\text{MoO}_3$  with space group  $Pbnm$  and unit cell parameters  $a = 13.86$   $\text{\AA}$ ,  $b = 3.70$   $\text{\AA}$  and  $c = 3.96$   $\text{\AA}$ , which can be indexed to standard spectrum given in JCPDS: 00-005-508. The orthorhombic  $\alpha$ - $\text{MoO}_3$  has a layered atomic structure comprising of double layers of  $\text{MoO}_6$  octahedra held together by two different bonds - covalent bonds in the ‘a’ and ‘c’-axes, i.e.,  $(h00)$  and  $(00l)$  directions and van der Waals bond in the ‘b’-axis, i.e.,  $(0k0)$  direction. The nature of the Mo–O bond changes considerably with the equilibrium bond distance, and varies from strongly covalent for the shortest bond to predominantly ionic for the longest bonds in the  $\text{MoO}_6$  octahedron. Consequently,  $\alpha$ - $\text{MoO}_3$  can form a variety of elongated morphologies (rods, wires, belts, tubes etc.) owing to this unusual crystal structure that favours anisotropic growth.<sup>8, 20, 32, 41, 42</sup>

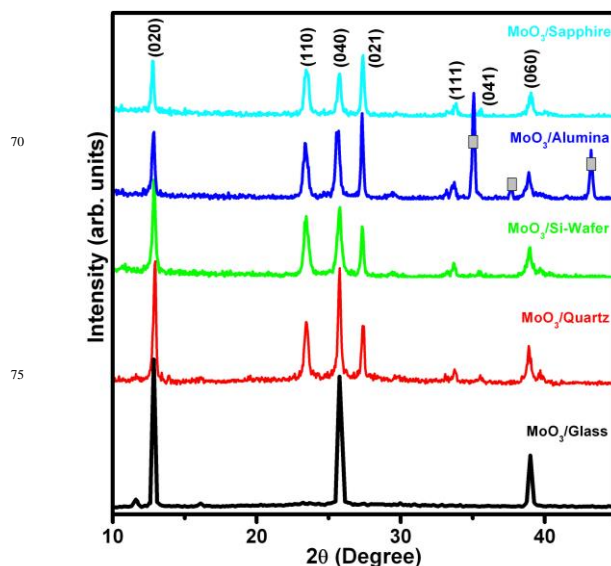


**Fig. 3** GIXRD patterns of the  $\text{MoO}_3$  nanostructures grown on various substrates. The shaded peaks on the alumina substrate belong to  $\text{Al}_2\text{O}_3$ .

The nanostructures on all substrates exhibit three well marked peaks  $(020)$ ,  $(040)$  and  $(060)$  indexed to orthorhombic  $\alpha$ - $\text{MoO}_3$  indicating the anisotropic growth of nanorods in  $(0k0)$  direction. Moreover this preferential orientation shall give lower interfacial energy and much higher nucleation rate resulting in the adsorption and accommodation of the atoms in that particular direction  $(0k0)$ . In addition to  $(0k0)$  peaks, the nanostructures except on glass substrate show many other diffraction peaks, indicating the poor  $b$ -axis orientation of these nanostructures. However, the thick vertical nanorods on alumina and nanoslabs on sapphire exhibit prominent peak at  $(021)$ , indicating their preferential growth orientation along  $(021)$  which is similar to those reported for the relatively large  $\text{MoO}_3$  nanobelts.<sup>8, 43</sup> The  $\text{MoO}_3$  nanoslabs/belts are grown generally as single crystalline having a principal growth direction along  $\langle 001 \rangle$  and the sideways growth along  $\langle 100 \rangle$ . The  $\langle 010 \rangle$  planes and  $\langle 100 \rangle$  planes enclose the nanobelt facets along the longitudinal direction, and the  $\langle 001 \rangle$  planes enclose the tips. The nanoslabs with a large width-to-thickness ratio are formed due to the large difference in close-packing rate (growth rate) between the  $\langle 010 \rangle$  plane and the  $\langle 100 \rangle$  plane in the orthorhombic  $\text{MoO}_3$  structure.<sup>8, 43</sup>

During film deposition and post-deposition treatments, there is always a possibility of the development of strain/stress, which affects the mechanical properties of the films such as stability of the microstructure, adhesion between the film and substrate and opto-electronic properties of the deposited films.<sup>44</sup> This internal stress, strain, lattice distortion or defects can broaden the XRD peaks so that the mean grain size estimated using the Debye Scherrer formula can be smaller than the actual value.<sup>45, 46</sup> Therefore in this paper, Williamson-Hall (W-H) method is employed to calculate the particle size and lattice strain. The effect of crystallite size and strain on the full widths at half maximum (FWHM) of the XRD peaks can be studied using W-H plot<sup>47</sup>

$$\beta \cos \theta = \frac{k\lambda}{D'} + 2\eta \sin \theta \quad (1)$$

where  $D'$  is the actual particle size,  $k$  is the correction shape factor which can be taken as unity and  $\eta$  is the residual strain. A plot of  $\beta \cos \theta$  versus  $\sin \theta$  (W-H plot) for the films is shown in Fig 4. The lattice strain in the films can be calculated from the slope of the plot and the actual particle size in the film can be estimated from the  $y$ -intercept of the plot. The calculated parameters are tabulated in Table 1.

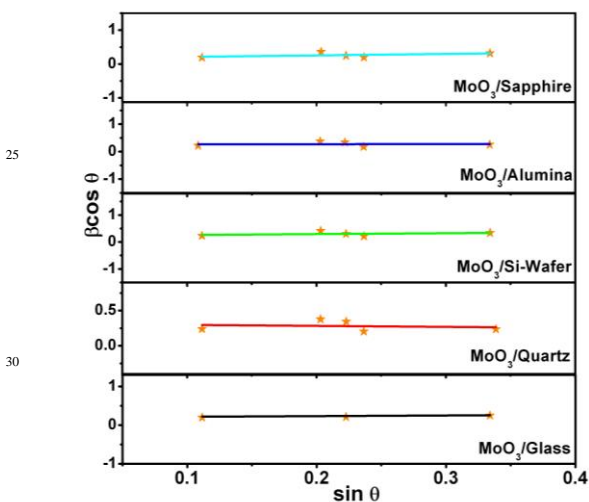


Fig. 4 Williamson-Hall plot for MoO<sub>3</sub> nanostructures grown on various substrates.

From the strain analysis it can be inferred that the shape and orientation of the nanostructures are depended on the strain formed in the films during crystal growth. The nanostructures formed on all the substrates except quartz exhibit tensile strain, on quartz, the well-aligned nanorods show compressive strain. The lesser strained nanorods on glass substrate are not well aligned whereas the nanorods are orientated on quartz substrate which may be due to the compressive strain formed in the film. The very less strained film on alumina show perpendicular growth of nanorods and the film on sapphire with higher strain exhibit nanoslabs. The formation of long nanowires on Si-wafer can be due to high tensile strain formed owing to the large lattice mismatch of MoO<sub>3</sub> nanorods to Si-wafer compared to other substrates.

The stress/strain induced nucleation caused by the thermal expansion coefficient mismatch and lattice mismatch between the MoO<sub>3</sub> film layer and the substrates may also be responsible for the diverse morphologies and orientations of the nanostructures.

Thermal mismatch between MoO<sub>3</sub> film and the substrates can be accounted from the shift of the centre of diffraction peaks compared to the standard JCPDS card [Ref. Code: 00-005-508]. The thermal expansion coefficient of the MoO<sub>3</sub> crystal ( $4.2 \times 10^{-5} \text{ C}^{-1}$ ) is higher than that of all the substrates ( $10^{-6}$ - $10^{-7} \text{ C}^{-1}$ ), which in turn cause the substrates to give a tensile stress to the film layer<sup>48</sup> as the substrate cools down from 400 °C to room temperature after the calcination process. This may be the reason for the uneven growth morphology of nanostructures on different substrates. The formation of well aligned nanorods on the quartz substrate can be attributed to the low value of thermal expansion coefficient ( $5.9 \times 10^{-7} \text{ C}^{-1}$ ) compared to glass ( $4.6 \times 10^{-6} \text{ C}^{-1}$ ) which induces high tensile stress to align the nanorods. The high tensile stress formed due to high value of thermal expansion coefficient of Si wafer ( $2.6 \times 10^{-6} \text{ C}^{-1}$ ) may be the reason for the formation of elongated nanowires. The values of expansion coefficients of alumina ( $8.1 \times 10^{-6} \text{ C}^{-1}$ ) and sapphire ( $7.59 \times 10^{-6} \text{ C}^{-1}$ ) are comparable which may contribute equivalent strains, results in the formation of thick nanostructures on these substrates. Since the shape of nanorods got modified during the controlled annealing process, the presence of a temperature gradient between the film and the substrate may favour the growth of low dimensional nanostructures during the growth process.<sup>42</sup>

The large shift of  $2\theta$  values of the XRD peaks to lower angles in crystalline substrates compared to the amorphous substrates is most probably due to the MoO<sub>3</sub> lattice expansion caused by the lattice mismatch between the MoO<sub>3</sub> and crystalline substrates. The amorphous nature of glass and quartz allows to exclude the effect of strain generated from the lattice mismatch which can act as a driving force for the generation of defects. The lattice mismatch between MoO<sub>3</sub> and the crystalline substrates (Si-wafer, alumina and sapphire) may be the reason for the change in morphology of the nanostructures on these substrates compared to those formed on amorphous glass and quartz. The unstrained lattice parameters of orthorhombic MoO<sub>3</sub> have been reported to be  $a = 0.3963$ ,  $b = 1.386$  nm and  $c = 0.3696$  nm. The  $a$ -axis lengths of Si-wafer, alumina and sapphire are 0.543 and 0.476 and 0.4785 nm respectively. The lattice mismatch is defined as<sup>49</sup>

$$I = \left[ \frac{(a_s - a_f)}{a_f} \right] \times 100\% \quad (2)$$

where  $a_s$  and  $a_f$  are the unstrained lattice (intrinsic) parameters of the substrate and film respectively. The lattice mismatch of crystalline MoO<sub>3</sub> oriented along the  $c$ -axis with Si Si-wafer, alumina and sapphire is 77.02%, 20.11% and 20.06%, respectively. This lattice mismatch can develop residual stresses in the crystal as well as at the substrate interface. In order to reduce the strain developed due to high lattice mismatch, the nanocrystals have to rotate an angle through a better lattice matching direction. Chang et al.<sup>50</sup> reported that the MoO<sub>3</sub> nanocrystals grown on Si-wafer rotate 'a'-axis 27° away from the Si [100] in order to reduce the mismatch by 2.2 %. The formation of longer nanowire bundles aligned in different directions on Si-wafer substrate may be due to the high lattice mismatch. Since the values of lattice mismatch of alumina and sapphire to MoO<sub>3</sub> are similar, the extreme difference in surface roughnesses can be accounted for the variation in growth orientations of nanocrystals in these substrates.

**Table 1** The morphological, structural and optical parameters of the MoO<sub>3</sub> nanostructures formed on different substrates.

Substrates	Thermal conductivity of substrates (W/mK)	Surface roughness of substrates (nm)	Thin film thickness (nm)	Thin film roughness (nm)	Particle size (nm)	Strain	Band gap (eV)
Glass	1.2	~17	385	25	38	0.1661	3.87
Quartz	1.4	~8	367	26	28	-0.1399	3.72
Si-wafer	125	~1	272	51	30	0.3214	3.66
Alumina	30	~60	401	8	31	0.0410	3.75
sapphire	40	~3	344	22	32	0.4347	3.63

5

Compared to the other substrates, high surface roughness and structure defects due to polycrystalline nature of alumina may favour the columnar growth of nanorods. The surface roughness and defects in the substrate surface can influence the shape and orientation of nanostructures as it governs the chemical adsorption, subsequent adhesion, nucleation and growth.<sup>51, 52</sup> Higher surface roughness of alumina substrates can offer higher surface area to the MoO<sub>3</sub> layer, especially at the convex areas of the surface. The alumina substrate with highest value of roughness has the lowest calculated value of strain from XRD analysis. This implies that the surface roughness plays a more critical role than the strain for the perpendicular growth of MoO<sub>3</sub> nanorods. Park et. al. have reported the influence of high surface roughness on the vertical growth of ZnO nanorods.<sup>53</sup> Moreover, the poor *b*-axis orientation observed for the Si-wafer, alumina and sapphire substrates is due to the large lattice mismatch. So the choice of an appropriate substrate is crucial to obtain highly *b*-axis oriented MoO<sub>3</sub> thin films.

From Table 1, it can be seen that the surface roughness of the substrates have profound influence on the film thickness and orientation of the nanostructures formed. The very low thickness of the films over Si-wafer may be due to poor adhesion of MoO<sub>3</sub> over the smooth surface (low roughness), which may contribute to the high tensile strain formed in the film. Interestingly, the substrate with highest surface roughness abides the films with lower rms roughness. The very low surface roughness may affect the film density and hence the thickness. Lower film thickness values appeared to be associated with smoother film surfaces. The adhesion energy between the film and the substrate atoms is provided by the vander Waal (physiosorption) forces, chemical interactions (chemisorptions) and exchange of charge across the film-substrate interface.<sup>54</sup>

The role of thermal conductivity (*k*) of the substrates on the formation of nanostructures also has to be considered as the '*k*' values are highly diverse in magnitude. The thermal conductivity values of the substrates obtained from data sheet are given in Table 1. The substrates having higher *k* facilitate the growth of long nanowires (on Si-wafer) and nanoslabs (on sapphire), however, the lower *k* substrates show short nanorods (on glass and quartz), implying that the mobility of particles and crystalline growth of the nanostructures are highly reliant on the *k* of the substrates. Moreover, the film on Si-wafer (maximum *k*) shows lowest film thickness and maximum film surface roughness. An et.al.<sup>55</sup> demonstrated that thermal conduction effects of the substrates can dictate the growth of the nanostructures, especially the 1D columnar structure growth as observed in the case of alumina substrate.

### 3.2. X-ray Photoelectron Spectroscopy (XPS) Studies

X-ray photoelectron spectroscopy (XPS) is employed to identify the stoichiometry of the nanostructures formed on different substrates. XP spectra for all MoO<sub>3</sub>/substrate combinations have been recorded. Fig 5 shows the XP survey (a) and core level (b) spectra of the MoO<sub>3</sub> crystals on alumina substrate. The XP Mo 3d core level spectrum is a simple spin-doublet with the Mo 3d<sub>3/2</sub> and Mo 3d<sub>5/2</sub> binding energies at 235.53 eV and 232.39 eV, respectively, corresponding to those of formal hexavalent molybdenum (Mo<sup>6+</sup>) ions.<sup>19, 56</sup> The XP O1s spectrum (Fig 5b) shows a most intense component at 530.33 eV assigned to the O<sup>2-</sup> ions of the oxide layer. The variation of peak position of Mo 3d and O1s core levels *w.r.t.* substrates are given in Table 2. The surface stoichiometry of the oxide films were calculated from the peak areas of Mo 3d and O1s spectra and are given in Table 2, which confirms the formation of MoO<sub>3</sub> and indicates the presence of O vacancies associated with the Mo<sup>5+</sup> defects.<sup>56</sup>

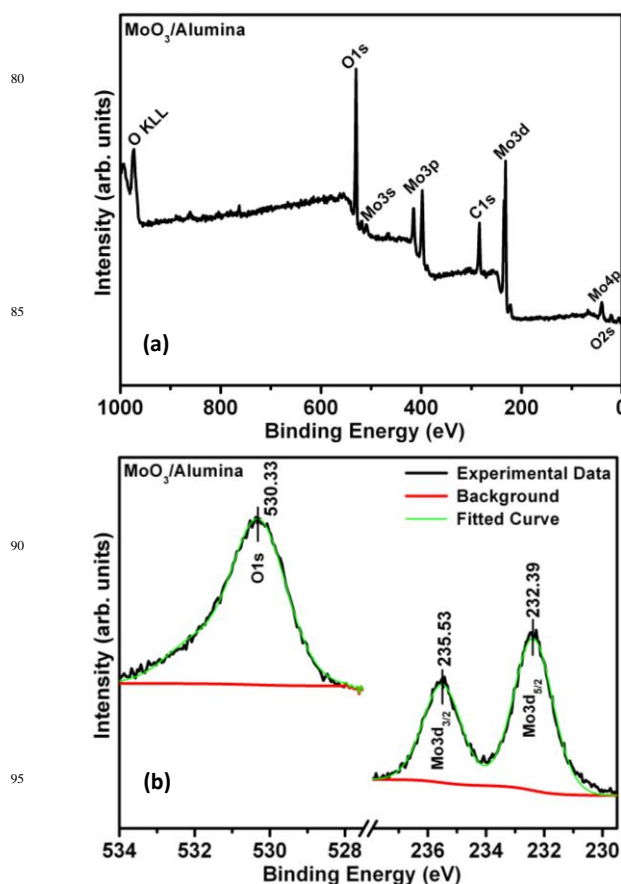


**Fig. 5** XP spectra of MoO<sub>3</sub> nanostructures on alumina substrate, (a) survey spectrum (b) O1s and Mo3d core level region.

**Table 2** Relative proportions of the components Mo and O and binding energy positions of the XP O1s, Mo3d Peaks.

Sample	Concentration (%)		Ratio O/Mo	Peak Position (eV)		
	Mo	O		O1s	Mo3d <sub>5/2</sub>	Mo3d <sub>3/2</sub>
MoO <sub>3</sub> /Glass	26.3	73.7	2.80	530.19	235.27	232.13
MoO <sub>3</sub> /Quartz	25.5	74.5	2.92	530.25	235.57	232.41
MoO <sub>3</sub> /Si-Wafer	25.6	74.4	2.91	530.41	235.64	232.51
MoO <sub>3</sub> /Alumina	25.9	74.1	2.86	530.33	235.53	232.39
MoO <sub>3</sub> /Sapphire	26.3	73.7	2.80	530.29	235.57	232.41

### 3.3. Micro-Raman Analysis

In order to investigate the vibrations of Mo and O atoms in the nanocrystals on different substrates, micro-Raman measurement is performed at room temperature. Typical micro-Raman spectrum of the MoO<sub>3</sub> nanostructures on different substrates is shown in Fig 6. The Raman intensity of the nanorods formed on the glass and quartz substrates is very high compared to those of nanostructures on the other substrates indicating the improved crystallinity of the nanorods on these substrates. The position of the Raman bands depends on the nature of the substrates and the peak shifts are related to changes in the force constants of the bonds (bond lengths) due to strain induced according to the nature of the substrates, i.e., positive and negative peak shifts correspond to larger and smaller force constants, respectively.<sup>57</sup> The expected Raman modes for orthorhombic MoO<sub>3</sub> and its comparison to the modes of nanostructures along with the corresponding symmetry and vibration assignments are given in Table 3. The observed Raman bands are assigned according to the single crystal study of Py et al.<sup>58, 59</sup> All the nanostructures show sharp and strong bands at ~ 996, 820 and 666 cm<sup>-1</sup>, and several weak bands corresponds to characteristic nature of orthorhombic  $\alpha$ -MoO<sub>3</sub> phase<sup>60</sup> which is consistent with the XRD analysis.

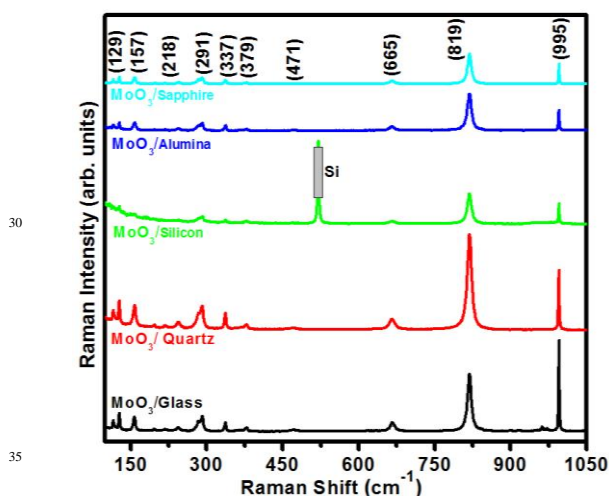


**Fig. 6** Micro-Raman patterns of the molybdenum oxide nanostructures on different substrates. Given assignments of the band positions are belonging to MoO<sub>3</sub>/sapphire, however, the variation of band positions with respect to the substrates are tabulated in Table 2.

Vibrational analysis by micro-Raman spectra reveals that the bands around the 1000–600 and 600–400 and below 200 cm<sup>-1</sup> are due to stretching, deformation and lattice modes respectively. The

presence of these bands shows the distorted nature of octahedra in the nanorods and can be assigned to the Mo<sup>6+</sup>=O stretching mode of terminal oxygen atoms, which are created from breaking of Mo<sub>2</sub>-O<sub>(1)</sub> bonds at the corner-shared oxygen. The sharp peak at 996 cm<sup>-1</sup> is assigned to the anti-symmetric stretching mode of terminal oxygen (Mo<sup>6+</sup> = O<sub>(1)</sub>) along the 'a' and 'b' axis which results from an unshared oxygen and it is responsible for the layered structure of  $\alpha$ -MoO<sub>3</sub>. The narrow shape of this band is attributed to the unshared terminal oxygen, O<sub>(1)</sub>.<sup>61</sup> The highest intensity of the Raman band at 996 cm<sup>-1</sup> by the nanorods on glass substrate compared to the nanostructures on other substrates may be due to enhanced polarizability of the electron cloud of the asymmetric stretching bond.

The nanorods on glass substrate exhibit two very low intense vibration bands at 902 cm<sup>-1</sup> and 953 cm<sup>-1</sup> which are characteristic of the monoclinic  $\beta$ -MoO<sub>3</sub> phase.<sup>1, 62</sup> Both the results indicate broken symmetry of octahedra introduced by the oxygen defects. The strong broad peak at ~ 820 cm<sup>-1</sup> is assigned to the doubly coordinated oxygen (Mo<sub>2</sub>-O<sub>(3)</sub>) symmetric stretching mode which results from corner-shared oxygen which is common to two MoO<sub>6</sub> octahedra. A possible cause of broadening of this intense band is due to the different degree of crystallisation of the samples and the lower oxygen/metal ratios. In the present case, the thermal treatments are performed in air and the non-stoichiometry is expected to be negligible. The higher the concentration of oxygen vacancies the shorter the lifetime of the excited state should be and could, therefore, lead to a broadening of the Raman bands.<sup>63</sup> Moreover, in the case of nanostructures, the phonon momentum selection rule  $q \approx 0$ , specific to the Raman scattering in ordered systems is no longer valid as the phonons are confined in space and all the phonons over the Brillouin zone will contribute to the first order Raman spectra.

The weight of the off-centre phonons increases as the crystal size decreases and the phonon dispersion causes an asymmetrical broadening and the shift of the Raman peaks.<sup>64</sup> The peak at 671 cm<sup>-1</sup> is assigned to the triply coordinated oxygen (Mo<sub>3</sub> - O<sub>(2)</sub>) stretching mode which results from edge-shared oxygens in common to three MoO<sub>6</sub> octahedra.<sup>65</sup> The band centred at ~ 471 cm<sup>-1</sup> corresponds to the Mo-O stretching and bending mode of MoO<sub>6</sub> octahedra. Raman bands observed in the 400–200 cm<sup>-1</sup> range (378, 338, 290, 246, 219, and 198 cm<sup>-1</sup>) correspond to various bending modes of the orthorhombic MoO<sub>3</sub> crystal which are tabulated in Table 3. In addition, the band at ~ 159 cm<sup>-1</sup> is assigned to the lattice mode and two weak bands at 218 and 245 cm<sup>-1</sup> represent the bending mode of Mo<sub>2</sub>-O<sub>(2)</sub>.

### 3.4. Diffuse Reflectance Studies

Diffuse reflectance spectroscopy (DRS) has been employed to determine the dispersion and band gap properties of the nanostructures on different substrates, by considering the spectral dependence of the diffuse reflectance data.<sup>66, 67</sup> DR UV-Vis spectra recorded in the range of 200–500 nm is as shown in Fig 7a. It can be seen that the nature of the substrate has a significant effect on the optical light absorption/dispersion properties of the nanostructures. The high reflectance from the layer on alumina may be due to the opaque nature of the base alumina substrate and high thickness of the film. The spectral shape dependency



**Table 3** Comparison of reported Raman bands with observed bands for nanostructures and their vibrational assignments. <sup>49-51</sup>

$\alpha$ -MoO <sub>3</sub> reported <sup>51</sup>	Raman bands (cm <sup>-1</sup> )					Assignments
	Non-oriented nanorods on glass	Oriented nanorods on quartz	nanowires on Si-wafer	Vertically oriented nanorods on alumina	Nanoslabs on sapphire	
995	996	996	994	995	995	$\nu_{as}$ Mo=O <sub>(1)</sub> Stretch
	953					Mo <sup>6+</sup> = O <sub>(1)</sub> stretch
819	820	820	818	819	819	$\nu_s$ Mo-O <sub>(3)</sub> -M Stretch
666	668	665	663	666	665	$\nu_s$ Mo-O <sub>(2)</sub> -Mo Stretch
473	473	469		471	471	$\nu_{as}$ O <sub>(2)</sub> -Mo-O <sub>(2)</sub> Stretch & bend
379	378	376	377	378	379	$\delta$ O <sub>(2)</sub> -Mo-O <sub>(2)</sub> Scissor
338	337	337	337	337	337	$\delta$ O <sub>(3)</sub> -Mo-O <sub>(3)</sub> bend
291	290	291	291	289	291	$\delta$ O <sub>(1)</sub> =Mo=O <sub>(1)</sub> Wagging
246	246	245	243	244	245	$\tau$ O <sub>(2)</sub> =Mo=O <sub>(2)</sub> twist
217	220	218		215	218	Rotational rigid MoO <sub>4</sub> chain mode, R <sub>c</sub>
198	197	197	183	197	196	$\tau$ O <sub>(2)</sub> =Mo=O <sub>(2)</sub> twist
158	156	159	159	156	157	Transitional rigid MoO <sub>4</sub> chain mode, T <sub>b</sub>
129	127	129	129	126	129	Transitional rigid MoO <sub>4</sub> chain mode, T <sub>c</sub>
116	115	115		114	115	Transitional rigid MoO <sub>4</sub> chain mode, T <sub>c</sub>

of the nanostructures indicates the molecular defect structures present in the films. The molecular migration and the formation of different Mo species over various substrates have already been revealed by DRS study.<sup>68, 69</sup>

$$\left[ \frac{h\nu}{2t} \ln \left( \frac{R_{\max} - R_{\min}}{R - R_{\min}} \right) \right]^{1/2} = A(h\nu - E_g) \quad (3)$$

where A is a constant which is different for different transitions,  $R_{\max}$  and  $R_{\min}$  are the maximum and minimum reflectance in reflection spectra and R is the reflectance for any intermediate energy photons recorded by the spectrophotometer. As in case of absorption spectra, a graph is plotted between  $[\ln(R_{\max} - R_{\min}) / (R - R_{\min})]^{1/2}$  (as ordinate) and  $h\nu$  (as abscissa), a straight line is obtained. The extrapolation of straight line to  $[\ln(R_{\max} - R_{\min}) / (R - R_{\min})]^{1/2} = 0$  axis gives the value of the direct band gap. The calculated band gap values (Table 1) of the films prepared on glass and quartz substrates are consistent with those values obtained from the optical absorption data by the Tauc plot method.<sup>66</sup> The variation of band gap values with respect to the substrate material designate the presence of defect structures in the band structure contributing the overall band gap. The band gap values show no linear dependence on the thickness, strain and roughness of the films. However, it is noticed that the film having highest particle size shows the highest band gap energy and can be attributed to the band bending effect at the grain boundaries as depicted in<sup>38</sup>. Also, the most strained film formed on sapphire substrate exhibit the lowest band gap energy, which is in accordance with the literature observation.<sup>70</sup> Srikant *et al.*<sup>71</sup> accounted the band gap narrowing of ZnO films on sapphire substrate based on the strain-induced deformation of potentials of ZnO.

### 3.5. Photoluminescence Studies

The room-temperature PL spectra (recorded at 250 nm) of MoO<sub>3</sub> nanostructures grown on various substrates under same growth conditions are shown in Fig 8. The excitation energy (250 nm / 4.97 eV) used is higher than the band gap energy (3.19-3.62 eV), so it is easy for an electron in the valence band to be directly excited to the conduction band; moreover, it is likely to be excited to the localised levels within the forbidden gap. It is found that the geometry of the nanostructures and nature of the substrates drastically affect the PL peak position and PL intensity. The morphology dependent PL behaviour may be due to the

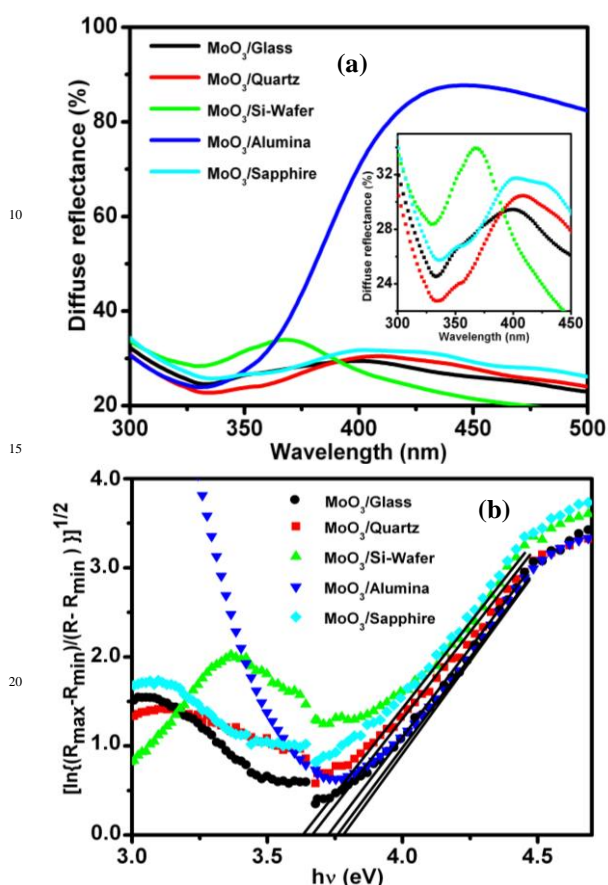


**Fig. 7** (a) Diffuse reflectance spectra of MoO<sub>3</sub> nanostructures on different substrates, inset: magnified view of the low intense curves and (b) Tauc plots showing possible fits to obtain the band gap.

The DRS curves of all substrates show absorption edge at the same spectral range, however, slightly varies according to the band gap energy. The band gap values are calculated using the formula,<sup>66, 67</sup>

variation in the confinement of carriers in small volume of different shaped nanostructures.<sup>72</sup> The positions of the PL bands and PL intensity vary according to the nature of the substrates.

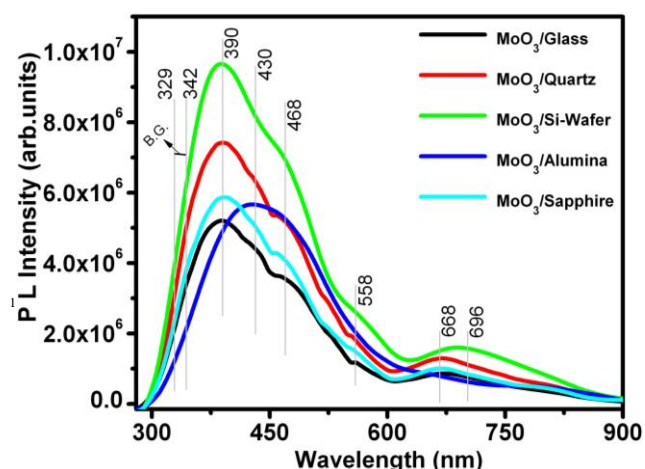


Fig. 8 PL spectra of MoO<sub>3</sub> nanostructures on different substrates excited at 250 nm.

15

The nanowires on the Si-wafer exhibit strong PL emission whereas the non-oriented tiny nanorods on the glass show the weak PL intensity. The stronger PL intensity exhibited by the nanowires on Si-wafer compared to those of the nanocrystals on other substrates are due to various factors such as high surface to volume ratio, large lattice mismatch and high surface roughness of the film. The bundled nanowires can offer large absorption cross section to the incident light due to high surface area, it eventually helps to enhance carrier confinement (nanorods increases the localization depth of the radially confined carriers) and strain-relaxation effects and hence shows better PL emission. High difference in the lattice mismatch induces elastic strain in the interfacial layer during the initial stage of growth and might affect their optical properties. The enhancement of PL intensity with increase in porosity and roughness may be accounted by the increase in surface area, which allows for strong absorption of incoming ultraviolet light. Whereas a smooth film results in specular reflection, a rough film may allow the excitation beam to be reflected onto another portion of the film surface, resulting in more efficient use of the excitation energy and hence superior PL intensity.<sup>73</sup> The films with low surface roughness show moderately low PL intensity, likely due to a combination of reflection of the incident light and total internal reflection. The high PL intensity of oriented nanorods on quartz compared to those of the nanostructures on glass, alumina and sapphire may be due to the oriented nature of the nanorods, which in turn gives the effect of nanowires. The lesser PL intensity exhibited by the nanorods on glass substrate may be due to its tilted orientation, which may reduce the orbital overlapping between nanorods and hence reduces radiative recombinations.

The PL spectra of all the samples show strong emission between 300-600 and a weak intense emission band in 600-800. Since the calculated value of band gap energy of MoO<sub>3</sub> nanostructures is between 3.63eV (342 nm) and 3.77 eV (329 nm), the other PL bands might be attributed to radiative decay of self-trapped exciton or linked to lattice imperfections such as simple oxygen vacancy or more complex defect centres, the

50

clustering of oxygen vacancies or the lower valence Mo<sup>5+</sup> ion associated with an oxygen vacancy as neighbour.<sup>41, 42, 74</sup> The oxygen vacancies are speculated to play a significant role for the PL emission from MoO<sub>3</sub> nanostructures. XPS studies revealed the presence of oxygen vacancies in the nanostructures formed on all substrates. An oxygen vacancy can distort MoO<sub>6</sub> octahedra by displacing Mo atom in the direction of the terminal oxygens. This lattice perturbation determines the energetic position of the defect states with respect to the valence band and the conduction band. In the distorted octahedra of orthorhombic MoO<sub>3</sub>, the central Mo ion's *d* levels get split into discrete energy levels, because of the crystal field effect. Upon excitation, the transition between these levels gives rise to excitonic emission bands. So the transitions at the visible region may be attributed, in the crystal field model, to the Mo<sup>5+</sup> *d-d* band transition of a heavily distorted polyhedron (Mo-O) in an octahedral crystal field.<sup>75, 76</sup> The detailed discussion on the splitting of electronic energy levels is given elsewhere.<sup>75-78</sup> The bands in the emission spectrum between 390 nm (3.18 eV) and 430 nm (2.89 eV) can be attributed to the hexa-coordinated [MoO<sub>6</sub>]<sup>5+</sup> *d<sub>z<sup>2</sup></sub>* - d<sub>yz</sub> transitions. The bands 468 nm (2.65 eV) and 558 nm (2.22 eV) can be attributed to the Mo<sup>5+</sup> penta-coordinated [MoO<sub>5</sub>]<sup>5+</sup> *d<sub>yz</sub> - d<sub>xz</sub>* and deep level Mo<sup>5+</sup> IVCT (Inter Valance Charge Transfer) transitions respectively. The bands between 668 nm (1.89 eV) and 696 nm (1.78 eV) may arise due to penta-coordinated [MoO<sub>5</sub>]<sup>5+</sup> *d<sub>yz</sub> - d<sub>xy</sub>* transitions. The intensity of this IVCT band is strongly dependent on the degree of oxidation, i.e., both fivefold-coordinated Mo<sup>5+</sup> and six fold-coordinated Mo<sup>6+</sup> are required. An IVCT transition involves optical transfer of an electron from one cation to another.<sup>79, 80</sup> PL studies, hence, shed light into the electronic structure and vacancy defects present in the MoO<sub>3</sub> nanostructures.

### 3.6. Gas Sensing Studies

MoO<sub>3</sub> has been recognized as an effective material for gas sensing applications.<sup>80-85</sup> The feasibility of using the nanostructures prepared on alumina substrates as gas sensitive material has been investigated with five different gases. Sensing element (Fig. 9b) comprising sensor chip and nanostructured MoO<sub>3</sub> sensitive layer (Fig. 9a, schematic) is developed as described in <sup>84, 85</sup>. The sensor is operated at 300 °C under the analyte exposure sequence over time given in Fig. 10 and more details concerning the measurement set up can be found in <sup>84, 85</sup>.

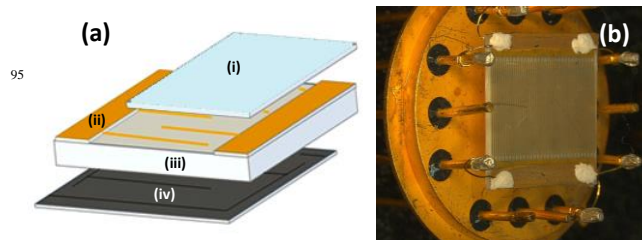
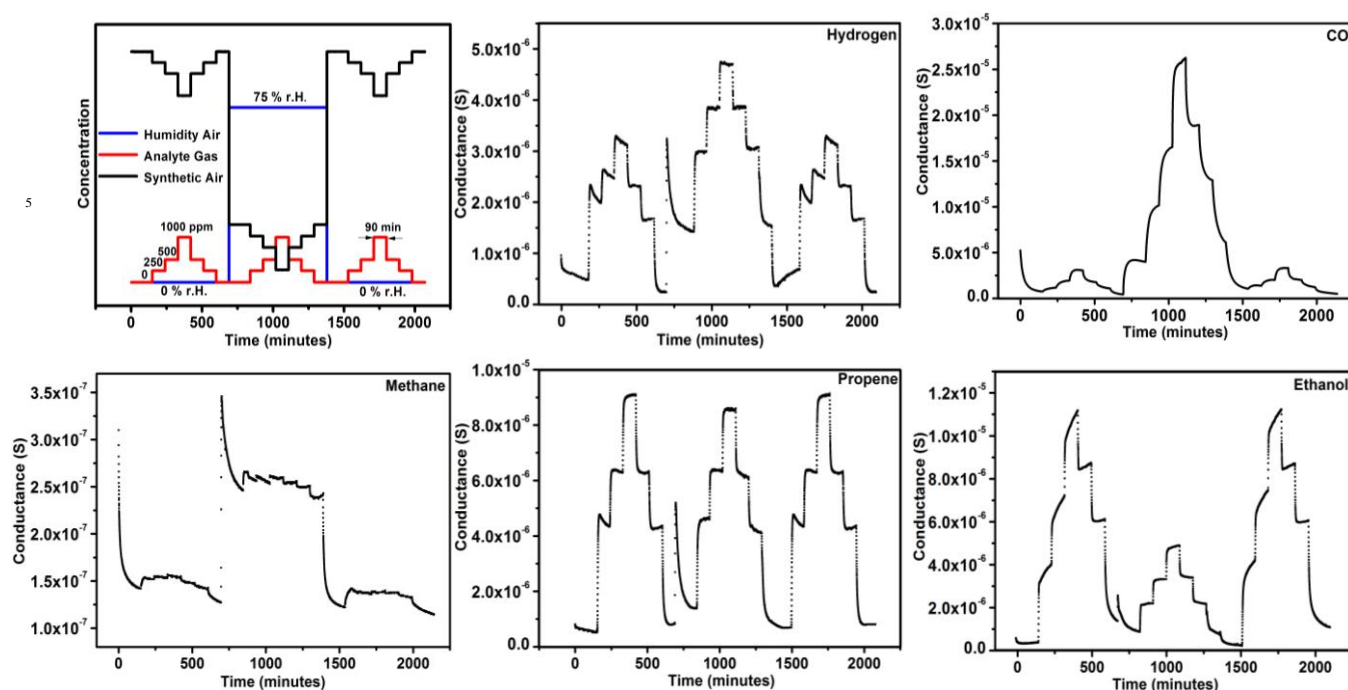


Fig. 9 (a) Schematic of the sensor chip with - (i) gas sensitive MoO<sub>3</sub> layer, (ii) Au IDE (60 fingers, having IDE-spacing: 60 μm and finger length: 4.825 mm), (iii) alumina substrate (7 mm × 7 mm) and (iv) thin film Pt-heater structure on reverse side. (b) Final sensing element with TO-8 header.

The responses of the MoO<sub>3</sub> layer towards five different gases and the variation of sensitivity for different concentrations at different humid conditions are illustrated in Fig. 10 and 11.

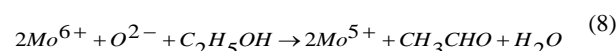
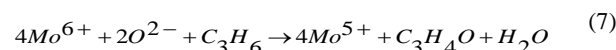
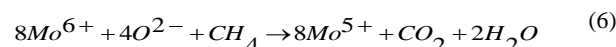
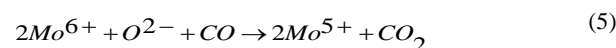
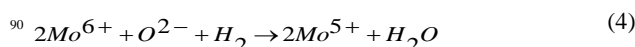
105



**Fig.10** Gas exposure sequence over time and corresponding sensor response to various gases at different concentrations under non-humid and humid (75 % r.H. at 21°C) ambiances. Operating temperature is 300 °C.

The sensor responses in terms of conductance change are very appealing with respect to the gases exposed at various operating conditions (Fig. 10). At the stepwise changes of the concentration, H<sub>2</sub> and propene responses display good reversibility at both non-humid and humid conditions. For ethanol and hydrogen, the sensor shows more stable performance at humid ambience than at non-humid situation, however, for CO the humid ambience resulted in high sensitivity with poor stability. Moreover, the sensor signal features seem to be reproducible at repeated gas exposure sequence of the same analyte concentration at non-humid conditions. For H<sub>2</sub> (also for methane), the sensing response at non-humid and humid conditions is comparable (Fig. 10 & 11), indicating that the presence of even high humid ambience does not affect the sensing performance. However, the presence of humid atmosphere has a dramatic influence on the sensor performance to CO and ethanol; the sensitivity enhances enormously for CO and diminishes drastically for ethanol (Fig. 10 & 11). For propene, the presence of humidity diminishes the sensitivity but not drastically as seen in the case of ethanol. Out of the gases, ethanol shows highest response at non humid conditions, however, at humid conditions CO has the highest sensitivity (Fig 11). The high response of the layer towards CO in the presence of humidity involves the competitive reactions between CO and H<sub>2</sub>O with the sensing layer occurring simultaneously on the surface.<sup>84</sup> The increase in conductance on exposure of CO in the presence of water indicates that the reduction process of the layers is also activated by the co-adsorption of CO with water.<sup>86</sup> The reduction of sensor signal to ethanol and propene at humid atmosphere can be attributed to the available oxide sites precluding nature of hydroxyl groups and induced desorption of adsorbed analyte species by water, both reduces the catalytic oxidation of analytes over MoO<sub>3</sub>.<sup>84,85</sup>

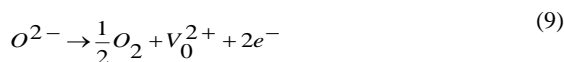
The gas detection mechanism of MoO<sub>3</sub> is not well established as there are only a few studies reported on the same. In general, the sensitivity action of semiconducting oxides towards reducing gases is concerned with the reaction of chemisorbed and/or lattice oxygen in the outermost surface layers. It is reported that the gas detection by MoO<sub>3</sub> mainly directs by the lattice oxygen rather than chemisorbed oxygen, which is different from other metal oxides- SnO<sub>2</sub> or ZnO etc.<sup>83, 87, 88</sup> The lattice oxygen from MoO<sub>3</sub> layer catalytically oxidizes the analyte gas and simultaneously reduces which determines the change in conductivity. If the catalytic oxidation of the reducing gas by lattice oxygen from the surface layer proceeds fast enough, the prevailing equilibrium is effectively perturbed and a new non-equilibrium state can be established that is characterized by a kinetically determined decrease in the concentration of negatively ionized surface layer oxygen species. As a consequence, mobile charge is formed in the oxide layer which can give rise to modifications in the electrical resistance of the material.<sup>88, 89</sup> Hence, this type of catalytic activity can lead to gas sensing process. The possible reactions taking place at the surface of MoO<sub>3</sub> for the gases under investigation are given by the following relations.<sup>85, 90</sup>



50

where,  $O^{2-}$  represents an unstable oxygen atom in an oxygen site at the surface.  $Mo^{6+}$  and  $Mo^{5+}$  represent respectively the valance states of Mo atom in  $MoO_3$  before and after exposure of gas. The adsorbed gas species and the desorbing by-products of the catalytic reactions are given in the right and left side of the gas reaction representations, respectively.

Hence, the gas detection process involves the reaction of the semiconducting bulk of  $MoO_3$  by consuming near-surface oxygen, this would lead to the partial oxidation of analyte gas and the formation of near-surface oxygen vacancies. A typical oxygen vacancy formation resulted in releasing electrons as given in <sup>91</sup>



That is, as a semiconductor becomes partially reduced by the removal of lattice oxygen, the conductance increases because the number of electron carriers increases in the catalyst. <sup>19, 83-85</sup>

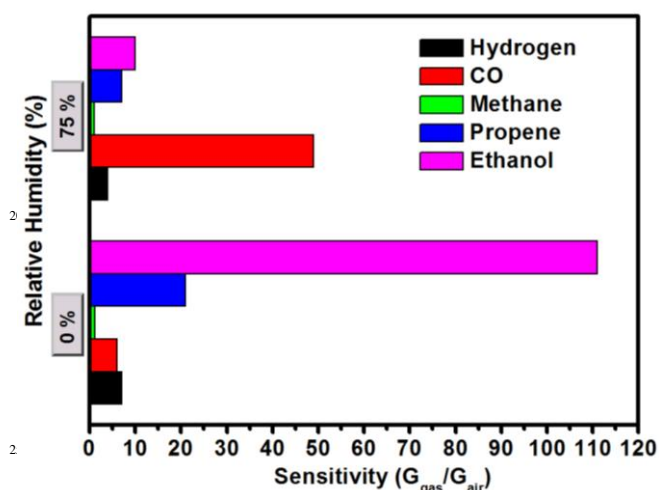


**Fig. 11** Variation of sensor response for 1000 ppm of different gases at non-humid and humid (75% r.H. at 21°C) ambiances.

The  $MoO_3$  nanostructured thin film layer on alumina substrate in the present work shows significantly comparable or even superior sensing performance to the works previously reported for various metal oxide systems. <sup>92-95</sup>

#### 4. Concluding remarks

The influence of substrate material on the morphological, structural and optical properties of  $MoO_3$  nanostructures is systematically investigated by growing layers on five different substrates; glass, quartz, Si-wafer, alumina and sapphire. The surface roughness, lattice parameters and thermal expansion coefficient of the substrates have profound influence on the morphology and various properties of the  $MoO_3$  nanostructures. The morphology, dimension and orientation of the nanostructures are drastically altered by the nature of substrates. Non-aligned nanorods, aligned nanorods, bundled nanowires, vertical nanorods and nanoslabs are formed respectively on the glass, quartz, Si-wafer, alumina and sapphire substrates. All the nanostructures formed on different substrates are crystallized with orthorhombic  $\alpha$ - $MoO_3$  layered structure, however, XPS study revealed the presence of oxygen vacancies in the films. Lattice strain calculation reveals that the nanostructures formed on all substrates except quartz exhibit tensile strain, the

compressive strain formed on quartz may be responsible for the well-aligned nanorods. The vibrational analysis of the nanostructures is carried out by micro-Raman analysis. Diffuse reflectance spectroscopy (DRS) has been employed to determine the energy band gap of the nanostructures on different substrates by considering the spectral dependence of the diffuse reflectance data. The substrate dependent PL emission exhibited by the films is also discussed in detail. The gas sensing characterization results towards five different gases are presented along with possible sensing mechanisms.

#### 60 Acknowledgement

Dr. N. Illyaskutty would like to thank German Academic Exchange Service (DAAD) for the fellowship (PKZ: A/09/74480) given throughout the course of this work. The valuable support of UGC-DAE, CSR, Indore, India by providing XRD, AFM and micro-Raman facilities is acknowledged. We also thank Prof. Rainer Schwab, Faculty of Mechanical Engineering and Mechatronics, Karlsruhe University of Applied Sciences for SEM measurements and Mrs. Angela Brauch for her assistance in SEM measurements.

#### 70 Notes and references

1. T. Brezesinski, J. Wang, S.H. Tolbert and B. Dunn, *Nature Materials*, 2010, **9**, 146–151.
2. J. Philip, A. Punnoose, B. I. Kim, K. M. Reddy, S. Layne, J. O. Holmes, B. Satpati, P. R. LeClair, T. S. Santos and J. S. Moopera, *Nature Materials*, 2006, **5**, 298–304.
3. Z.R. Tian, J.A. Voigt, J. Liu, B. Mckenzie, M.J. Mcdermott, M.A. Rodriguez, H. Konishi and H. Xu, *Nature Materials*, 2003, **2**, 821–826.
4. M.T. Greiner, L. Chai, M. G. Helander, W. Tang and Z.-H. Lu, *Advanced Functional Materials*, 2013, **23**, 215–226.
5. J. Zhou, S.Z. Deng, N.S. Xu, J. Chen and J.C. She, *Appl. Phys. Lett.*, 2003, **83**, 2653–2655.
6. J. S. Chen, Y. L. Cheah, S. Madhavi and X. W. Lou, *J. Phys. Chem. C*, 2010, **114**, 8675–8678.
7. S. Hu and X. Wang, *J. Am. Chem. Soc.*, 2008, **130**, 8126–8127.
8. M.E. Kurtoglu, T. Longenbach and Y. Gogotsi, *J. Mater. Chem.*, 2011, **21**, 7931–7936.
9. K. Dewangan, N.N. Sinha, P.K. Sharma, A.C. Pandey, N. Munichandriah and N. S. Gajbiye, *Cryst.Eng.Comm.*, 2011, **13**, 927–933.
10. L. Cheng, M. Shao, X. Wang and H. Hu, *Chem. Eur. J.*, 2009, **15**, 2310–2316.
11. X. M. Wei and H. C. Zeng, *J. Phys. Chem. B*, 2003, **107**, 2619–2622.
12. S.H. Lee, Y.H. Kim, R. Deshpande, P.A. Parilla, E. Whitney, D.T. Gillaspie, K.M. Jones, A.H. Mahan, S.B. Zhang and A.C. Dillon, *Adv. Mater.*, 2008, **20**, 3627.
13. G. Li, L. Jiang, S. Pang, H. Peng and Z. Zhang, *J. Phys. Chem. B*, 2006, **110**, 24472–24475.
14. C. V. Krishnan, J. Chen, C. Burger and B. Chu, *J. Phys. Chem. B*, 2006, **110**, 20182–20188.
15. K.P. Chang, U.S. Chen and H.C. Shih, *Electrochemical and Solid State Letters*, 2007, **10**, H111–H113.
16. T. Liu, Y. Xie and B. Chu, *Langmuir*, 2000, **16**, 9015–9022.
17. A. Khademi, R. Azimirad, A.A. Zavarian and A.Z. Moshfegh, *J. Phys. Chem. C*, 2009, **113**, 19298–19304.
18. B. Yan, Z. Zheng, J. Zhang, H. Gong, Z. Shen, W. Huang and T. Yu, *J. Phys. Chem. C*, 2009, **113**, 20259–20263.
19. M. M. Y. A. Alsaif, K. Latham, M. R. Field, D. D. Yao, N. V. Medehkar, G. A. Beane, R. B. Kaner, S. P. Russo, J. Z. Ou and K. Kalantar-zadeh, *Advanced Materials*, 2014, **26**, 3931–3937.
20. K. Kalantar-zadeh, J. Tang, M. Wang, K. L. Wang, A. Shailos, K. Galatsis, R. Kojima, V. Strong, A. Lech, W. Wlodarski and R. B. Kaner, *Nanoscale*, 2010, **3**, 429–433.

21. M.B. Rahmani, S.H. Keshmiri, J. Yu, A.Z. Sadek, L. Al-Mashat, A. Moafi, K. Latham, Y.X. Li, W. Wlodarski, and K. Kalantar-zadeh, *Sensors and Actuators B*, 2010, **145**, 13–19.
22. L. Mai, B. Hu, W. Chen, Y. Qi, C. Lao, R. Yang, Y. Dai and Z. L. Wang, *Adv. Mater.*, 2007, **19**, 3712–3716.
23. K. Chen, S. Xie, A. T. Bell and E. Iglesia, *Journal of Catalysis*, 2000, **195**, 244–252.
24. D. Y. Kim, G. Sarasqueta and F. So, *Solar Energy Materials & Solar Cells*, 2009, **93**, 1452–1456.
25. S. Balendhran, J. Deng, J. Z. Ou, S. Walia, J. Scott, J. Tang, K. L. Wang, M. R. Field, S. Russo, S. Zhuiykov, M. S. Strano, N. Medhekar, S. Sriram, M. Bhaskaran and K. Kalantar-zadeh, *Advanced Materials*, 2013, **25**, 109–114.
26. C.G. Granqvist, *Handbook of Inorganic Electrochromic Materials*, Elsevier, New York, 1995.
27. L. Zheng, Y. Xu, D. Jin and Y. Xie, *Chem. Mater.*, 2009, **21**, 5681–5690.
28. C.G. Granqvist, A. Azens, A. Hjelm, L. Kullman, G.A. Niklasson, D. Ronnov, M.S. Mattsson, M. Veszelei and G. Vaivars, *Solar Energy Materials & Solar Cells*, 1998, **63**, 199.
29. J. N. Yao, K. Hashimoto and A. Fujishima, *Nature*, 1992, **355**, 624–626.
30. C. Bechinger, S. Ferrere, A. Zaban, J. Sprague and B. A. Gregg, *Nature*, 1996, **383**, 608–610.
31. J. Z. Ou, J.L. Campbell, D. Yao, W. Wlodarski and K. Kalantar-zadeh, *J. Phys. Chem. C*, 2011, **115**, 10757–10763.
32. A. Michailovski, J.D. Grunwaldt, A. Baiker, R. Kiebach, W. Bensch and G. R. Patzke, *Angew. Chem. Int. Ed.*, 2005, **44**, 5643–5647.
33. Y.L. Xie, F.C. Cheong, Y.W. Zhu, B. Varghese, R. Tamang, A.A. Bettiol and C.H. Sow, *J. Phys. Chem. C*, 2010, **114**, 120–124.
34. K. Sakaushi, J. Thomas, S. Kaskel, and J. Eckert, *Chem. Mater.*, 2013, **25**, 2557–2563.
35. A. Pardo and J. Torres, *Thin Solid Films*, 2012, **520**, 1709–1717.
36. Y. H. Cho, Y. N. Ko, Y. C. Kang, Il-D. Kim and Jong-Heun Lee, *Sensors and Actuators B*, 2014, **195**, 189–196.
37. I. Navas, R. Vinodkumar, K.J. Lethy, A.P. Detty, V. Ganesan, V. Sathe and V.P. Mahadevan Pillai, *J. Phys. D: Appl. Phys.*, 2009, **42**, 175305.
38. I. Navas, R. Vinodkumar, K.J. Lethy, M. Satyanarayana, V. Ganesan and V.P. Mahadevan Pillai, *J. Nanosci. Nanotechnol.*, 2009, **9**, 5254–5261.
39. I. Navas, R. Vinodkumar and V.P. Mahadevan Pillai, *Appl Phys A*, 2011, **103**, 373–380.
40. M.L. Fuller, *J. Appl. Phys.*, 1944, **15**, 164.
41. X.K. Hu, D.K. Ma, L.Q. Xu, Y.C. Zhu and Y.T. Qian, *Chemistry Letters*, 2006, **35**, 962–963.
42. X. Chen, W. Lei, D. Liu, J. Hao, Q. Cui and G. Zou, *J. Phys. Chem. C*, 2009, **113**, 21582–21585.
43. Y. B. Li, Y. Bando, D. Golberg and K. Kurashima, *Appl. Phys. Lett.*, 2002, **81**, 5048–5050.
44. K.N. Tu and R. Rosenberg *Analytical techniques for thin films*, Academic Press, San Diego, 1988.
45. S.T. Tan, B.J. Chen, X.W. Sun, W.J. Fan, H.S. Kwok, X.H. Zhang and S.J. Chua, *J. Appl. Phys.*, 2005, **98**, 013505.
46. S. B. Qadri, J. P. Yang, E. F. Skelton and B. R. Ratna, *Appl. Phys. Lett.*, **70** (1997)1020.
47. G.K. Williamson and H. Hall, *Acta Metall.*, 1953, **1**, 22.
48. H. Negishi, S. Negishi, Y. Kuroiwa, N. Sato and S. Aoyagi, *Phys. Rev. B*, 2004, **69**, 064111.
49. R. C. Cammarata, *Progress in Surface Science*, 1994, **46**, 1–38.
50. W.C. Chang, X. Qi, J.C. Kuo, S. Lee, S.K. Ng and D. Chen, *Cryst. Eng. Comm.*, 2011, **13**, 5125–5132.
51. M. Riaz, A. Fulati, Q. X. Zhao, O. Nur, M. Willander and P. Klason, *Nanotechnology*, 2008, **19**, 415708.
52. K. Hosono, I. Matsubara, N. Murayama, S. Woosuck and N. Izu, *Chem. Mater.*, 2005, **17**, 349–354.
53. S.H. Park, S.Y. Seo, and S.H. Kim and S.W. Han, *Appl. Phys. Lett.*, 2006, **88**, 251903.
54. M. Ohring, *Material science of thin films deposition and structure*, Academic Press, San Diego, 2002.
55. W. An, D. D. Jiang, J. R. Matthews, N. F. Borrelli and P. Biswas, *J. Mater. Chem.*, 2011, **21**, 7913.
56. J. Ś. Mrowiecka, S. de Diesbach, V. Maurice, S. Zanna, L. Klein, E. Briand, I. Vickridge and P. Marcus, *J. Phys. Chem. C*, 2008, **112**, 11050–11058.
57. K. Ajito, L. A. Nagahara, D. A. Tryk, K. Hashimoto and A. Fujishima, *J. Phys. Chem.*, 1995, **99**, 16383–16388.
58. M.A. Py, Ph.E. Schmid and J.T. Vallin, *Nuovo Cimento B*, 1977, **38**, 271–279.
59. M.A. Py and K. Maschke, *Physica B*, 1981, **105**, 370–374.
60. M. Dieterle and G. Mestl, *Phys. Chem. Chem. Phys.*, 2002, **4**, 822–826.
61. I.R. Beattie and T.R. Gilson, *J. Chem. Soc. A: Inorg. Phys. Theor.*, 1969, 2322–2327.
62. E. M. McCarron III, *J. Chem. Soc., Chem. Commun.*, 1986, **198**, 336–338.
63. G. Mestl, N.F.D. Verbruggen, E. Bosch and H. Knözinger, *Langmuir*, 1996, **12**, 2961.
64. D. Bersani, P. P. Lottici and X. Z. Ding, *Appl. Phys. Lett.*, 1998, **72**, 73–75.
65. G.M. Ramans, J.V. Gabrusenoks, A.R. Lulis and A.A. Patmalnieks, *J. Non-Cryst. Solids*, 1987, **90**, 637–640.
66. M. Nowak, B. Kauch, and P. Sziperlich, *Rev. Sci. Instrum.*, 2009, **80**, 046107.
67. V. Kumar, S. K. Sharma, T.P. Sharma and V. Singh, *Optical Materials*, 1999, **12**, 115.
68. L. Mosqueira and G. A. Fuentes, *Mol. Phys.*, 2002, **19**, 3055–3057.
69. L. Mosqueira, S.A. Gomez and G. A. Fuentes, *J. Phys: Condens. Matter*, 2004, **16**, S2319–2327.
70. R. Shao, K. Zheng, B. Wei, Y. Zhang, Y. Li, X. Han, Z. Zhang and J. Zou, *Nanoscale*, 2014, **6**, 4936–4941.
71. V. Srikant and D. R. Clarke, *J. Appl. Phys.*, 1997, **81**, 6357–6364.
72. C.C. Hong, H. Ahn, C.Y. Wu and S. Gwo, *Optics Express*, 2009, **17**, 17227–17233.
73. M. Cich, K. Kim, H. Choi and S.T. Hwang, *Appl. Phys. Lett.*, 1998, **73**, 2116–2118.
74. M. Itoh, K. Hayakawa and S. Oishi, *J. Phys.: Condens. Matter*, 2001, **13**, 6853–6864.
75. M. Labanowska, *Phys. Chem. Chem. Phys.*, 1999, **1**, 5385.
76. M. Dieterle and G. Mestl, *Phys. Chem. Chem. Phys.*, 2002, **4**, 812–821.
77. D. Hanlon, C. Backes, T. M. Higgins, M. Hughes, A. O’Neill, P. King, N. McEvoy, G. S. Duesberg, B. M. Sanchez, H. Pettersson, V. Nicolosi, and J. N. Coleman, *Chem. Mater.*, 2014, **26**, 1751–1763.
78. L. X. Song, J. Xia, Z. Dang, J. Yang, L. B. Wang and J. Chen, *CrystEngComm*, 2012, **14**, 2675–2682.
79. T. R. Zhang, W. Feng, C. Y. Bao, R. Lu, X. T. Zhang, T. J. Li and Y. Y. Zhao, *J. Mater. Res.*, 2001, **16**, 2256–2263.
80. G. Mestl, *J. Raman Spectrosc.*, 2002, **33**, 333–347.
81. X. Wen, W. Yang, Y. Ding, S. Niu and Z. L. Wang, *Nano Research*, 2014, **7**, 180–189.
82. O. Lupan, V. Cretu, M. Deng, D. Gedamu, I. Paulowicz, S. Kaps, Y. K. Mishra, O. Polonskyi, C. Zamponi, L. Kienle, V. Trofim, I. Tiginyanu, and R. Adelung, *Journal of Physical Chemistry C*, DOI: 10.1021/jp5038415, 2014.
83. M.M.Y.A. Alsaif, S. Balendhran, M. R. Field, K. Latham, W. Wlodarski, J. Z. Ou and K. Kalantar-zadeh, *Sensors and Actuators B*, 2014, **192**, 196–204.
84. N. Illyaskutty, H. Kohler, T. Trautmann, M. Schwotzer and V.P. Mahadevan Pillai, *Sensors and Actuators B*, 2013, **187**, 611–621.
85. N. Illyaskutty, H. Kohler, T. Trautmann, M. Schwotzer and V. P. Mahadevan Pillai, *Journal of Materials Chemistry C*, 2013, **1**, 3976–3984.
86. N. Barsan and R. Ionescu, *Sensors and Actuators B*, 1993, **12**, 71–75.
87. E. Comini, L. Yubao, Y. Brando and G. Sberveglieri, *Chemical Physics Letters*, 2005, **407**, 368–371.
88. S.S. Sunu, E. Prabhu, V. Jayaraman, K.I. Gnanasekar, T.K. Seshagiri and T.Gnanasekaran, *Sensors and Actuators B*, 2004, **101**, 161–174.
89. P. Meuffels, *J. Eur. Ceram. Soc.*, 2007, **27**, 285–290.
90. A. Bielanski and J. Haber, *Oxygen in Catalysis*, Marcel Dekker, New York, 1991.
91. A.K. Prasad, D.J. Kubinski and P.I. Gouma, *Sensors and Actuators B*, 2003, **93**, 25–30.

- 
92. A. Z. Sadek, S. Choopun, W. Wlodarski, S. J. Ippolito, and K. Kalantar-zadeh, *IEEE Sensors Journal*, 2007, **7**, 919.
93. Z. Lou, L. Wang, T. Fei and T. Zhang, *New J. Chem.*, 2012, **36**, 1003–1007.
- 5 94. X. X. Zou, G. D. Li, P. P. Wang, J. Su, J. Zhao, L. J. Zhou, Y. N. Wang and J. S. Chen, *Dalton Trans.*, 2012, 41, 9773.
95. Z. Lou, J. Deng, L. Wang, T. Fei and T. Zhang, *RSC Adv.*, 2013, 3, 3131.

10

15

20

25

30

35

40